

## ARTICLE OPEN



# Low-pressure-driven special wettable graphene oxide-based membrane for efficient separation of water-in-oil emulsions

Nadeem Baig <sup>1✉</sup>, Ismail Abdulazeez<sup>1</sup> and Isam H. Aljundi <sup>1,2</sup>

Oil and water separation is a significant challenge due to the rapid discharge of oily wastewater. Special wettable membranes have received substantial consideration in emulsified oil/water separation. Here, a superhydrophobic octadecyl-functionalized crosslinked graphene-oxide-grafted ceramic membrane (R18-CLGO-N-CM) was designed to separate water-in-oil emulsions. The selective layer of the ceramic membrane was evaluated using molecular dynamics simulation studies to understand its mechanism and separation capabilities. The underwater oil contact angle on the surface of the R18-CLGO-N-CM was dramatically reduced, from  $141.3^\circ \pm 1.5^\circ$  to  $0^\circ$ , and the water contact angle in air increased from  $0^\circ$  to  $152.8^\circ \pm 0.6^\circ$ , after functionalization. High hexane permeability was observed in the range of 294 to 311  $\text{L m}^{-2} \text{h}^{-1}$ . The octadecyl-functionalized crosslinked graphene oxide acts as an excellent separating layer to selectively allow oil passage with a separation efficiency of ~99% for water-in-oil emulsion. The designed membranes show excellent antifouling behavior while dealing with water-in-heavy oil emulsions. The surface of the functionalized membrane was restored with a flux recovery ratio of 98.5% by simply treating the surface with dichloromethane while separating the water-in-light oil emulsions. This work shows that the rational functionalization and grafting of 2D materials on the membrane surface can significantly enhance the antifouling characteristics and the separation performance of the membranes.

*npj Clean Water* (2023)6:40; <https://doi.org/10.1038/s41545-023-00252-y>

## INTRODUCTION

Wastewater consisting of emulsified oil and water mixtures is commonly released from several mainstream industries, including petrochemical, steel, textile, food, and leather<sup>1</sup>. Discharging oily wastewater into freshwater bodies without proper treatment is a significant environmental hazard and a deep concern for ecosystem sustainability. Oil extraction sites are also a substantial contributor to oily wastewater. In order to enhance oil recovery and force oil to the surface, extra water is injected into oil reservoirs, which produces oil-containing water. The produced water is discharged into a water body or reinjected, bringing complex environmental challenges<sup>2</sup>. Furthermore, oil quality is directly affected by its water content, and the presence of water in oil is a critical industrial challenge<sup>3</sup>. Therefore, oil/water mixtures must be investigated to enhance the efficiencies of industries and to preserve ecosystems from the negative impact of oil.

Several conventional methods are used to separate oil/water mixtures. These methods include centrifuges, depth filters, flotation, oil skimmers, settling tanks, and magnetic separation<sup>3</sup>. These methods are effective for separating immiscible oil and water mixtures; however, they seriously suffer during the separation of emulsions. Several other shortcomings are associated with conventional approaches, such as energy-intensive processes, sources of secondary contaminants, operational complexity, and poor separation efficiencies<sup>4</sup>. A significant challenge is associated with surfactant stabilized emulsions wherein the droplet size is so small that it is difficult to separate using conventional methods. Due to the inefficiencies of traditional techniques, new methods, and techniques are being investigated for efficient separation of oil/water emulsions<sup>5</sup>.

Membrane-based technologies have shown great potential for separating oil/water emulsions with high separation efficiency and low cost. The membrane-based process can be applied to purify

various industrial effluents<sup>6,7</sup>. As a result, several membranes that include microfiltration<sup>7</sup>, ultrafiltration<sup>8</sup>, and nanofiltration<sup>9</sup> have been used to separate oil/water emulsions. According to their base materials, membranes used for oil/water separation are classified as either polymeric or inorganic. Recently, ceramic membranes have received significant attention in separating oil/water emulsions due to their wear resistance, chemical inertness, controlled pore size, and temperature resistance<sup>10</sup>. Due to the abovementioned characteristics,  $\text{ZrO}_2$ <sup>11</sup>,  $\text{Al}_2\text{O}_3$ <sup>12</sup>, kaolin<sup>13</sup>, and  $\text{SiO}_2$ <sup>14</sup> have been extensively investigated for emulsion separation. In general, emulsions can be divided into two forms according to their continuous phase: (i) oil-in-water emulsions<sup>15</sup> and (ii) water-in-oil emulsions<sup>11</sup>.

The size exclusion principle is well known for separating solid particles, and membranes with controlled pore size provide excellent separation efficiency. However, separating the dispersed phase from an oil/water emulsion is complex as small emulsified droplets do not behave like solid particles. Under pressure, these emulsified droplets can be squeezed, deformed, and even passed through pores that are smaller than their size<sup>16</sup>. Therefore, a more advanced membrane design that rejects the dispersed phase is required based on wettability and the size exclusion principle. Because of this, more focus has been paid to fabricating membranes with special wettable surfaces<sup>17</sup>. Special wettable surfaces designed for oil/water separation are either superhydrophilic/underwater-superoleophobic<sup>18</sup> or superhydrophobic/superoleophilic<sup>19</sup>. Superhydrophilic/underwater-superoleophobic membranes are highly selective for water and suitable for treating oil-in-water emulsions<sup>20</sup>. Superhydrophobic and superoleophilic membranes are super selective for oil and strongly reject water<sup>21</sup>.

As mentioned earlier, ceramic membranes are suitable for separating oil/water emulsions. However, ceramic membrane surfaces are hydrophilic<sup>22</sup> and are most appropriate for separating oil-in-water emulsions<sup>23</sup>. For the separation of water-in-oil

<sup>1</sup>Interdisciplinary Research Center for Membranes and Water Security, King Fahd University of Petroleum and Minerals, Dhahran 31261, Saudi Arabia. <sup>2</sup>Chemical Engineering Department, King Fahd University of Petroleum and Minerals, Dhahran 31261, Saudi Arabia. ✉email: nadeembaig@kfupm.edu.sa

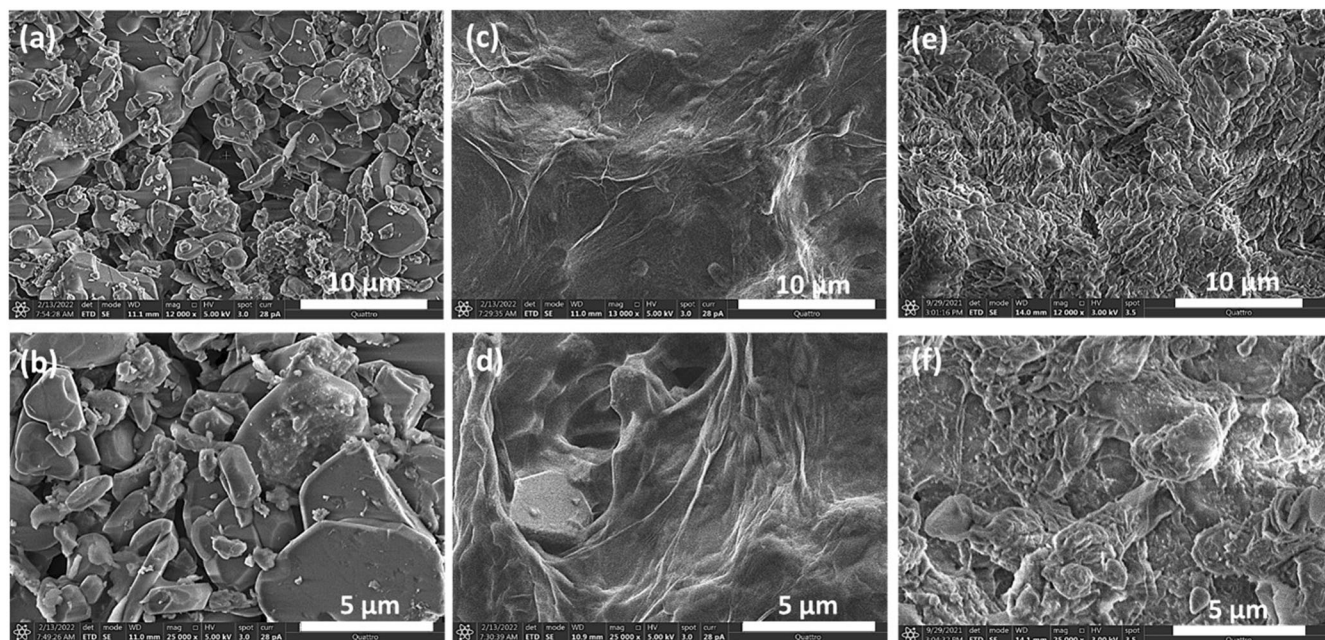


**Fig. 1** Field emission Scanning electron microscope images of the membranes. FE-SEM micrographs of the top-view of the different membranes (a, b) p-CM, (c, d) CLGO-N-CM, and (e, f) R18-CLGO-N-CM at two different magnifications.

emulsions, ceramic membranes are usually modified with a low surface energy material<sup>24</sup>. Ceramic membranes also operate under pressure. Therefore, there is a need to develop an effective barrier layer of low surface energy material, demonstrating both characteristics of size exclusion and special wettability. The grafting of a barrier layer with the features mentioned above has remained a significant challenge on ceramic membrane surfaces.

Membrane fouling is another challenge facing environmentally friendly membrane operation. During the separation process, the dispersed phase penetrates the porous membrane, which results in the blocking of the pores and the formation of a compact cake layer. Ultimately, it results in the irreversible fouling of the membrane, making it unsuitable for practical use. Fouling of membranes is inevitable<sup>25</sup>, but it is necessary to develop membranes that are easily reversible and operable at low pressure to prevent entrance of the dispersed phase into the membrane pores. Two-dimensional (2D) materials are an excellent choice for developing a separating layer with anti-fouling characteristics<sup>26,27</sup>. The stability of these 2D materials can be enhanced by grafting them onto the membrane surface. Herein, crosslinked graphene oxide sheets are grafted onto the surface of a ceramic membrane using N1-(3-Trimethoxysilylpropyl)diethylenetriamine, which provides an amine-rich surface. Graphene oxide, which is hydrophilic and unsuitable for separating water-in-oil emulsions, was immobilized on the N1-(3-Trimethoxysilylpropyl)diethylenetriamine grafted ceramic membrane. This CLGO-N-CM surface was chemically activated by grafting with a low surface energy material to produce an active layer that consists of R18-CLGO-N-. Separation efficiencies and anti-fouling behavior of the R18-CLGO-N-CM were thoroughly investigated for surfactant-stabilized water-in-oil emulsions.

## RESULTS AND DISCUSSION

### Morphological and elemental analyses of the ceramic membrane

In order to improve ceramic membrane performance for water-in-oil emulsions, pristine ceramic membranes were grafted with a

range of active groups to achieve a fully functionalized super-hydrophobic surface. The separating layer was developed with the help of the crosslinked graphene oxide, which was later functionalized with a long alkyl chain (R18) containing organosilicon. After each grafting step, the surface of the pristine ceramic membrane (p-CM) was significantly changed. The SEM was used to investigate the surface morphologies of pristine and functionalized ceramic membranes (Fig. 1). The images show a typical p-CM surface morphology, which consists of semicircle  $\text{Al}_2\text{O}_3$  particles that are irregularly accumulated to form an interconnected porous network. It was also observed that the porous p-CM network is insufficient to screen the surfactant stabilized water droplets for the water-in-oil emulsions as the pore size and surface chemistry are inappropriate for efficient separation. Therefore, graphene oxide is used as a separating layer. The graphene oxide layer is grafted on the surface of the ceramic membrane with the help of the N1-(3-Trimethoxysilylpropyl)diethylenetriamine. In the SEM images (Fig. 1c, d), nanosheets of graphene oxide have grown on the surface of the p-CM. The sheet acts as a barrier layer for the free passing of the oil/water emulsion. The graphene sheets were found well spread on the surface of the p-CM with some wrinkles, which generally appear on the graphene oxide to stabilize its layered structure.

Furthermore, the wrinkled graphene oxide provides more active sites and surface areas for interaction<sup>28</sup>. The discrete  $\text{Al}_2\text{O}_3$  particles, which were compressed to form a p-CM, are barely visible in the CLGO-N-CM. This indicates that it has been turned into a support layer, and the graphene oxide formed a barrier layer. It is well known that graphene oxide is hydrophilic and more selective toward water than oil; it can allow the slippage of water while separating water-in-oil emulsions. As a result, the activity of the crosslinked graphene oxide (CLGO) was significantly enhanced by functionalizing its surface with the  $\text{CH}_3(\text{CH}_2)_{16}\text{CH}_2 - (\text{R18}-)$ . In the morphological analyses of the R18-CLGO-N-CM, the  $\text{Al}_2\text{O}_3$  membrane surface was entirely changed compared to the p-CM, and distinctive changes were observed concerning the GO-N-CM. For example, the surface of the R18-CLGO-N-CM appeared rougher compared to the CLGO-N-CM and wavy in nature (Fig. 1e, f). It is well-documented that surface roughness plays a



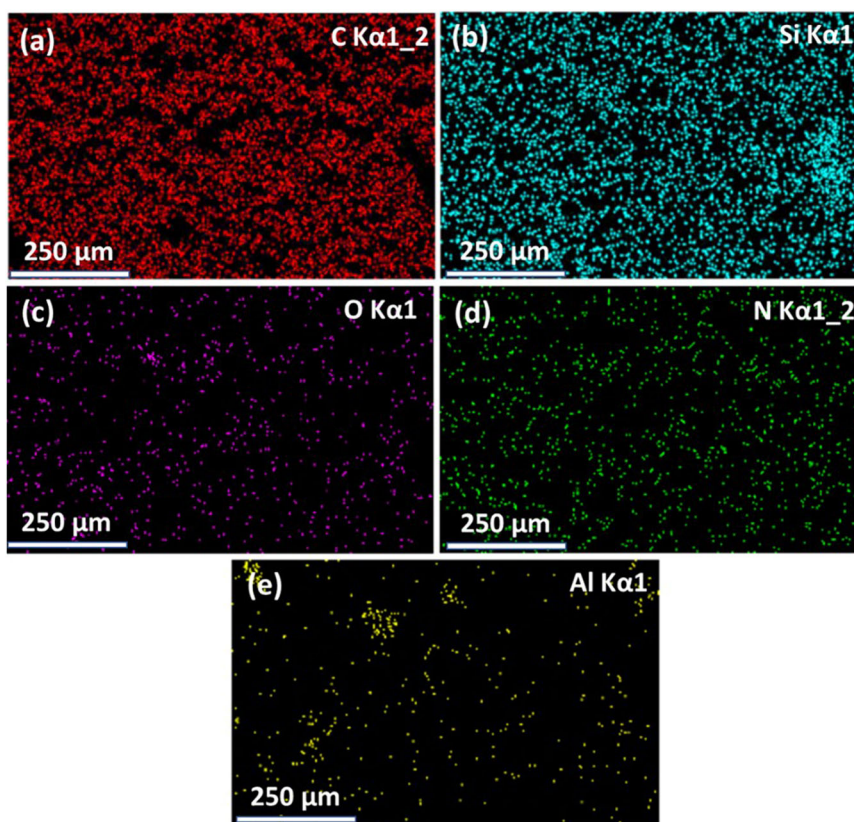


**Fig. 2 EDX mapping of the membrane.** Energy-dispersive X-ray mapping of the upper surface of the R18-CLGO-N-CM membrane. The individual EDX elemental mapping of the (a) C, (b) Si, (c) O, (d) N, and (e) Al shows their distribution in the separating layer of the membrane.

critical role in enhancing surface hydrophobicity<sup>29</sup>. The grafting of graphene oxide and R18- on the ceramic disc with the help of N1-(3-Trimethoxysilylpropyl)diethylenetriamine and glutaraldehyde produced a defect-free surface that is evident in the membrane morphology in Fig. 1e, f. The morphological changes that appeared after grafting GO and the R18- on the surface of the p-CM have strengthened the formation of special wettable ceramic membranes best suited to separate water-in-oil emulsions.

Elemental analyses provided further helpful information regarding the compositional changes before and after grafting OD-CLGO on the p-CM. It has been demonstrated that p-CM mainly consists of alumina particles that develop a randomly spread porous network. For the p-CM, energy-dispersive X-ray spectroscopy (EDX) shows the presence of Al, O, and Si, with no other prominent peaks (Supplementary Fig. 1). After grafting the N1-(3-Trimethoxysilylpropyl)diethylenetriamine, prominent peaks corresponding to C, N, and Si appeared, along with Al and O. This indicates that the N<sub>1</sub>-(3-Trimethoxysilylpropyl)diethylenetriamine interacted through the hydroxyl group present on the surface of the p-CM. Furthermore, the C contribution from the N1-(3-Trimethoxysilylpropyl)diethylenetriamine on the surface of the p-CM has become prominent in the EDX spectrum of N-CM (Supplementary Fig. 2). After graphene oxide grafting, the significant enhancement in the carbon content on the surface of the ceramic membrane has endorsed the presence of graphene oxide on the surface of the N-CM. This is evident through the SEM images, where the graphene oxide sheets were clearly observed on the surface of the ceramic membranes, which covers the surface of the alumina particles. The carbon percentage reached up to 61.7% after grafting with graphene oxide on the surface of the N-CM membranes (Supplementary Fig. 3). The organosilicon also has a long chain of 18 carbons, so functionalizing the

graphene oxide with it further enhances the percentage of carbon on the ceramic membrane surface. The carbon content on the surface of the R18-CLGO-N-CM reached up to 78.1%; the high concentration of carbon content is evident that the graphene oxide surface has been grafted with the long alkyl chains. Along with carbon, oxygen, and silicon also appeared as significant elements, with an elemental composition of 11.5 and 9.8%, respectively. The Al intensity and its percentage composition (0.6%) were substantially reduced, which shows better coverage of the porous surface of the ceramic membrane by the CLGO-OD grafted layer. The appearance of an intense Si peak in the R18-CLGO-N-CM EDX has also indicated that the n-octadecyl has been linked to graphene oxide through the Si, which results in the increased intensity on the surface of the ceramic membrane. The elemental mapping of R18-CLGO-N-CM also shows that the surface of the functionalized ceramic membrane is rich in carbon, silicon, and oxygen (Fig. 2).

#### FTIR analysis of ceramic membranes

In order to understand the various functionalities on the surface of the ceramic membranes, the surface of the R18-CLGO-N-CM was investigated using FTIR analysis in the region of 500–4000 cm<sup>-1</sup>. In pristine ceramic membranes, several prominent absorption bands appeared at certain wavenumbers, characteristic of alumina ceramic membranes. For example, the prominent band appeared at 1097 cm<sup>-1</sup> due to the  $\gamma$ -alumina Al–O vibration mode<sup>30</sup>. The absorption band at 1639 cm<sup>-1</sup> was assigned to the H–O–H scissor modes of physisorbed water<sup>31</sup>. The broad absorption band appeared in the range of 3261–3736 cm<sup>-1</sup> due to the hydroxyl groups bonding with the Al<sup>3+</sup> (Fig. 3a). These hydroxyl groups on the surface of the ceramic membranes provided an opportunity to link to the N1-(3-Trimethoxysilylpropyl)diethylenetriamine chemically. The broad

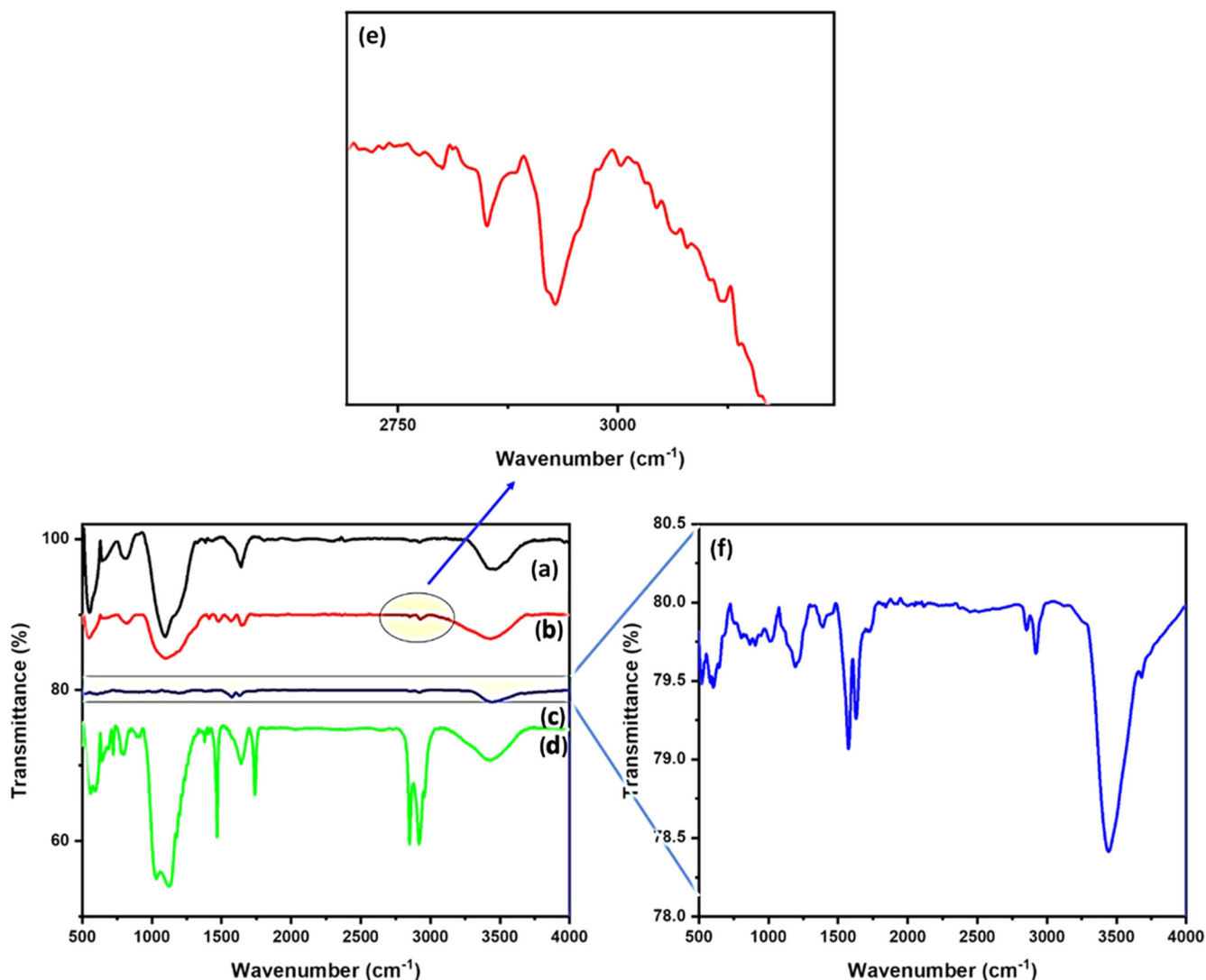


**Fig. 3** FTIR spectra of the membranes. **a** p-CM, **(b)** N-CM, **(c)** GO, and **(d)** R18-CLGO-N-CM. **e** The magnified spectrum of the encircled portion of the N-CM membrane in **(b)** and **(f)** The magnified spectrum of the graphene oxide.

absorption band in the range of  $951\text{--}1379\text{ cm}^{-1}$  contained information on the  $-\text{Si-O-Si-}$  and  $-\text{Si-O-Al}$  vibrations<sup>32</sup>.

The  $-\text{CH}$  stretching vibrations became prominent for the p-CM at  $2850\text{ cm}^{-1}$  and  $2928\text{ cm}^{-1}$ . Notably, in the FTIR spectra of the N-CM, the  $-\text{CH}$  stretching vibrations due to the  $-\text{CH}_3$  group are absent, as the N1-(3-Trimethoxysilylpropyl)diethylenetriamine linker contained only the methylene groups (Fig. 3b). This result indicates the successful introduction of the linker to the surface of the p-CM. The graphene oxide FTIR shows the typical characteristics peaks, illustrated in the magnified figure of the graphene oxide FTIR (Fig. 3c, f). For example, the alkoxy, epoxy, and carboxylic acid  $-\text{C-O}$  stretching vibrations were observed in the range of  $1000\text{--}1400\text{ cm}^{-1}$ <sup>33</sup>. The absorption band at  $1625\text{ cm}^{-1}$  was assigned to the aromatic  $-\text{C}=\text{C}-$  vibrations<sup>34</sup>. The carbonyl group ( $-\text{C}=\text{O}$ ) stretching vibrations were observed at  $1728\text{ cm}^{-1}$ , indicating the presence of the carboxylic group in the graphene oxide sheets<sup>35</sup>. A broad absorption band at  $3443\text{ cm}^{-1}$  appeared due to the hydroxyl groups present on the basal plane of the graphene oxide<sup>36</sup>. After the organosilicon  $\text{C}_{18}\text{H}_{37}\text{Cl}_3\text{Si}$  interacted with the CLGO-N-CM, an FTIR spectrum with prominent new absorption bands appeared after scanning the surface of the R18-CLGO-N-CM. The intensity and sharpness of the  $-\text{CH}$  absorption bands were substantially enhanced at  $2850\text{ cm}^{-1}$  and  $2918\text{ cm}^{-1}$ .

These stretching vibrations belong to the methylene groups. The long chain of the OD contained 17 methylene groups and ended with the methyl group. Therefore, a substantial enhancement in the peak intensity of the  $-\text{CH}$  vibrations was observed. The absorption band with reduced intensity observed at  $2950\text{ cm}^{-1}$  was due to the  $-\text{CH}$  stretching of the  $-\text{CH}_3$  group. The carbonyl group from the CLGO-N-CM absorption band appeared at  $1739\text{ cm}^{-1}$ . The appearance of the  $\text{Si-O}$  absorption band at  $1032\text{ cm}^{-1}$  endorsed the linking of the  $\text{C}_{18}\text{H}_{37}\text{Cl}_3\text{Si}$  with the CLGO-N-CM<sup>37</sup>.

#### AFM analysis of the ceramic membranes

Surface roughness is imperative in the performance of superhydrophobic membranes. Theoretically, the water contact angle on smooth surfaces cannot exceed  $120^\circ$ . However, micropatterned or microtextured surfaces can display an apparent contact angle greater than  $150^\circ$  and be related to superhydrophobic surfaces, impersonating the lotus leaf-like behavior. The p-CM membrane shows high roughness, as it consists of  $\text{Al}_2\text{O}_3$  particles; these particles produce numerous grooves and void pores, which result in high roughness. The average roughness ( $R_a$ ) and root mean square roughness ( $R_q$ ) of the p-CM were observed at  $0.53\text{ }\mu\text{m}$  and  $0.65\text{ }\mu\text{m}$ , respectively. The

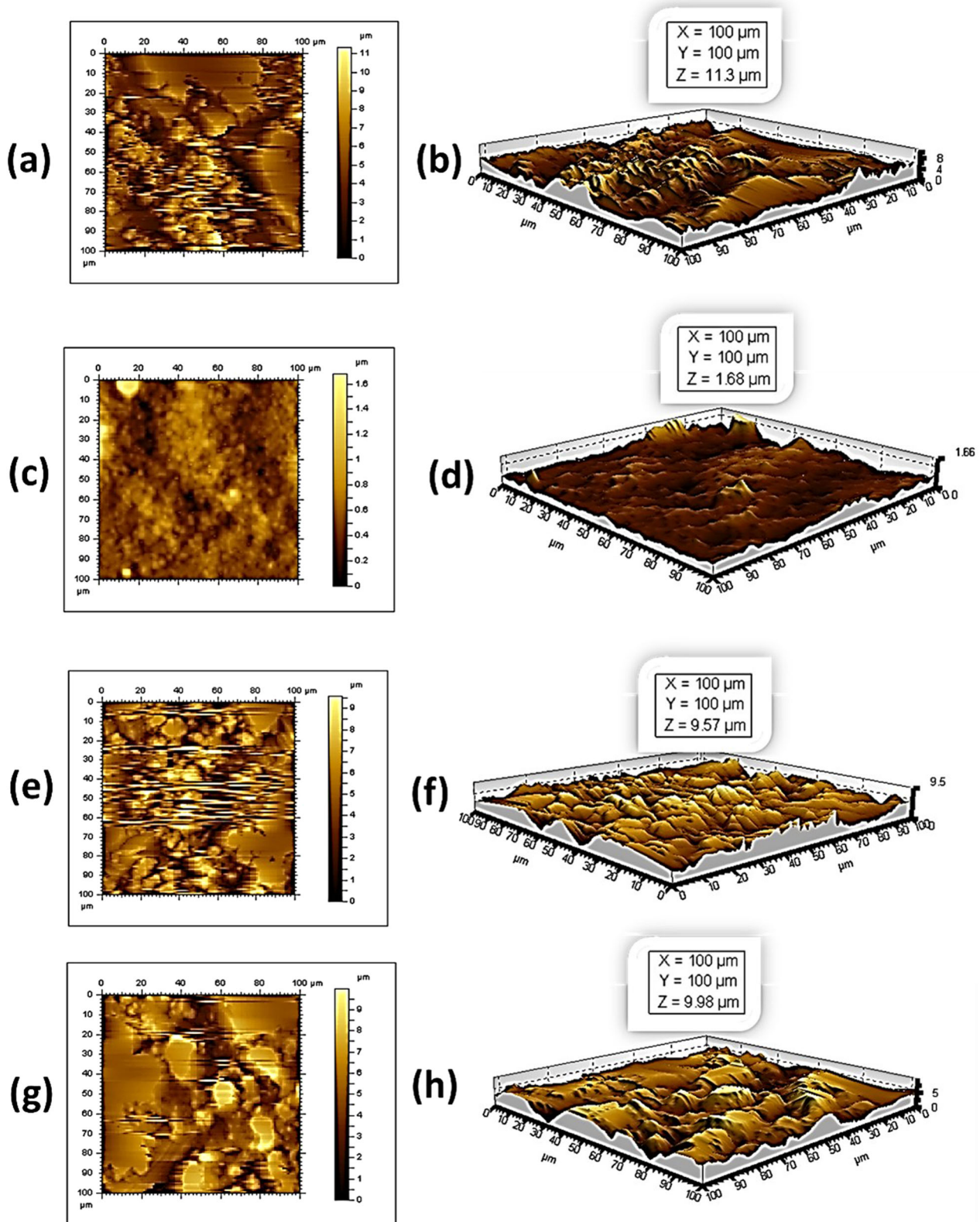


**Fig. 4 Atomic-force-microscopy topographic images of the membranes.** Two-dimensional and three-dimensional images of the membranes (a, b) p-CM, (c, d) N-CM, (e, f) CLGO-N-CM, and (g, h) R18-CLGO-N-CM.

presence of deep valleys and peaks is apparent in the 3D AFM image of the p-CM (Fig. 4b). Notably, after introducing the N1-(3-Trimethoxysilylpropyl)diethylenetriamine linker, the roughness decreased, and the valleys/peaks prominent in p-CM

became less pronounced than before due to the possible growth of the linkers into the valleys, making the surface partially smooth. The  $R_a$  and  $R_q$  of the N-CM were observed at about  $0.06 \mu\text{m}$  and  $0.07 \mu\text{m}$ , respectively (Fig. 4c, d). After



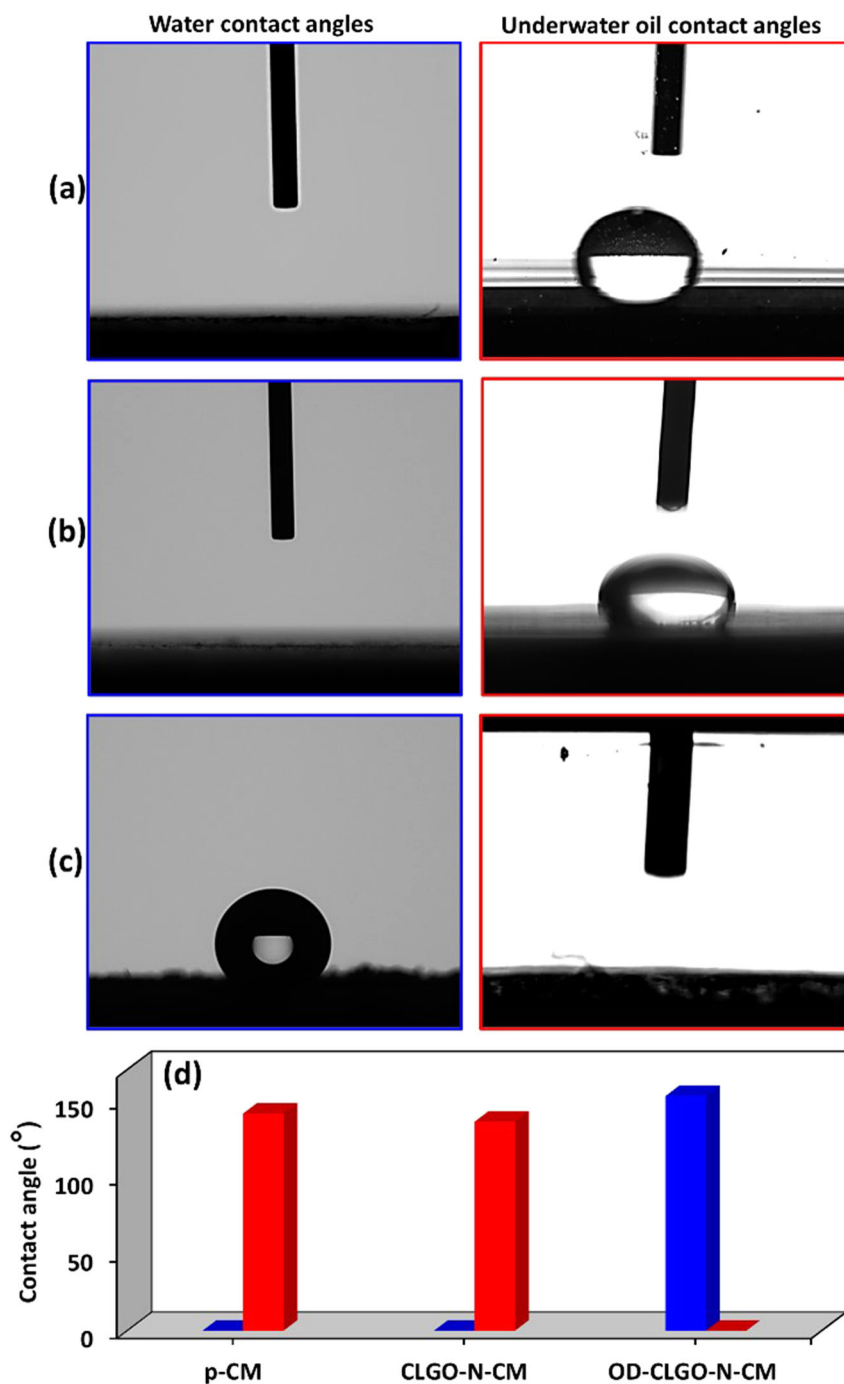


**Fig. 5 Surface wettability analysis of the membranes.** Water contact angles in air and underwater oil contact angles on the surface of the various membranes (a) p-CM, (b) CLGO-N-CM, and (c) OD-CLGO-N-CM. **d** Histograms show the water contact angles (blue color) and underwater oil contact angles (red color) on the surfaces of the membranes. The water and underwater oil contact angles were measured using the 5  $\mu$ l drop of liquid.

grafting the crosslinked graphene oxide on the N-CM surface, a significant enhancement in the surface roughness was observed ( $R_a = 0.591 \mu\text{m}$ ,  $R_q = 0.735 \mu\text{m}$ ) (Fig. 4e, f). The average surface roughness slightly decreased after introducing the long alkyl chain containing organosilicon. The  $R_a$  and  $R_q$  were found at  $0.572 \mu\text{m}$  and  $0.758 \mu\text{m}$ , respectively (Fig. 4g, h). Afterward, the water contact angle on the surface of the R18-CLGO-N-CM surpassed  $150^\circ$ , endorsing the high surface roughness of the membranes.

#### Evaluation of the wettability of the functionalized ceramic membranes

Surface wettability was imperative in the separation. The wettability of the smooth surface can be determined by using Young's model (Eq. 1)

$$\cos\theta = (\gamma_{SV} - \gamma_{SL})/\gamma_{LV} \quad (1)$$

where  $SV$ ,  $SL$ , and  $LV$  indicate the solid-vapor, solid-liquid, and liquid-vapor interface surface tension, respectively. The Wenzel

model (Eq. 2) was used to determine the wettability of the rough surfaces:

$$\cos\theta_w = r\cos\theta \quad (2)$$

where  $\theta_w$  is the Wenzel contact angle, and  $r$  indicates the roughness factor. The  $r$  is the ratio of the actual area to the geometrically projected area of the rough surface, which is normally greater than one. The hierarchical surface on which water cannot impregnate the rough surface at the solid–liquid interface due to the presence of air pockets, wettability, or the contact angle is best described using the Cassie–Baxter equation (Eq. 3).<sup>38,39</sup>

$$\cos\theta_c = rf\cos\theta + f - 1 \quad (3)$$

where  $f$  indicates the solid–liquid fraction under the contact area, and  $r$  represents the roughness ratio of the wet part of the solid surface. For separating the oil and water emulsions, surface chemistry is playing a significant role in achieving the desired separation efficiency. Specifically, such special wettable membranes are required to separate the water-in-oil emulsions, which are more favorable for oil than water. The membranes, which are superhydrophobic and superoleophilic in nature, are considered ideal for separating the water-in-oil emulsions as these membranes have a strong affinity for oil. The water drop was immediately spread on the surface of the p-CM as it encountered the membrane surface, showing the superhydrophilicity of the pristine ceramic membrane. Underwater, the p-CM showed no affinity for oil, and the oil contact angle was observed at about

$141.3^\circ \pm 1.5^\circ$ . This result indicates that the p-CM has no affinity for the oil and cannot be used for the selective permeation of the oil while separating the water-in-oil emulsions based on the special wettability.

The surface of CLGO-N-CM also appeared hydrophilic as the water drop slowly penetrated the membrane surface; some hydrophilicity might have been compromised on the graphene oxide surface due to its crosslinking with glutaraldehyde. However, the surface still appeared oleophobic underwater, with an oil contact angle of  $136.0^\circ \pm 0.4^\circ$ . The behavior of the ceramic membrane changed after interaction with the  $C_{18}H_{37}Cl_3Si$ . The surface of the R18-CLGO-N-CM turned superhydrophobic at a water contact angle above  $150^\circ$  (Fig. 5). After being crosslinked through the glutaraldehyde, the remaining hydroxyl group of the graphene oxide interacted with the  $C_{18}H_{37}Cl_3Si$ . This crosslinking produced a low-energy surface due to the long alkyl chain and consumption of the free hydroxyl groups of graphene oxide. The surface of the R18-CLGO-N-CM became superoleophilic, and the oil drop immediately spread on the R18-CLGO-N-CM surface underwater (Fig. 5c). The oil drop does not usually spread underwater, except it makes contact with low surface energy materials. The R18-CLGO-N-CM surface is the perfect choice due to the presence of long alkyl chains on the CLGO, which forms a separating layer on the ceramic membrane surface.

The behavior of the oil drop underwater on the p-CM surface is shown in Fig. 6 and Supplementary Video 1. The p-CM membrane surface moved slowly and was pushed toward the oil drop. However, the oil drop showed no affinity for the surface and

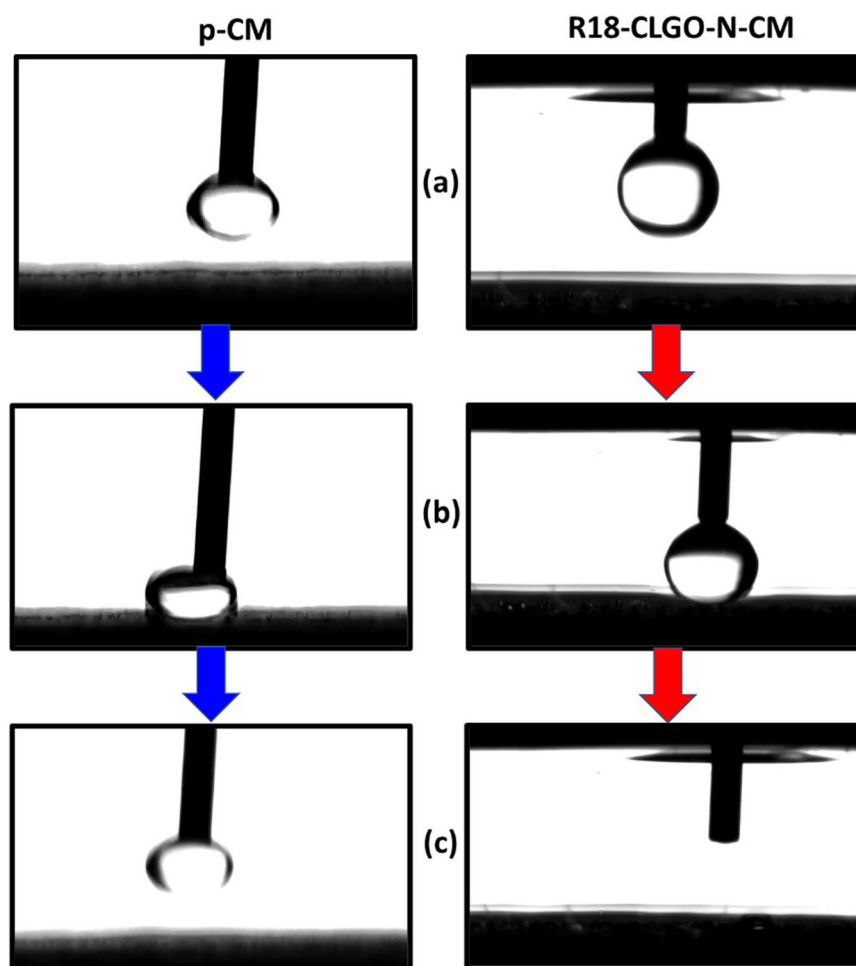


**Fig. 6 Behavior of oil drops underwater on the surface of the membranes.** The images were captured at various positions of oil drops from the membrane surfaces (a) oil drop underwater, (b) oil drop approach the membrane surface, (c) drop behavior after touching the surface.

stayed with the needle of the automated syringe. Figure 6c shows that the oil drop remained with the syringe needle when the p-CM surface moved away from it. Supplementary Video 1 shows that surface repelled the oil drop, which provides an ample chance for the passage of water while separating the water-in-oil emulsions and makes it unfavorable for separating water-in-oil emulsions. However, when the surface of the p-CM functionalized with the R18-CLGO-N, the behavior of the surface toward the water and oil changed. Figure 6 and Supplementary Video 2 show that as the surface of the R18-CLGO-N-CM membrane approached the oil drop, oil drop immediately disappeared from R18-CLGO-N-CM surface and spread rapidly underwater on the surface of the functionalized membrane. It is well known that a heavy oil drop remains circular underwater and does not spread; thus, the spreading on the surface of the R18-CLGO-N-CM membranes was only due to its superoleophilic nature. The long alkyl chains tend to turn hydrophilic surfaces into hydrophobic surfaces with the proper functionalization strategy. For instance, the hydrophilic MOF, UiO-67, is turned into the hydrophobic UiO-67-Rs after introducing the alkyl chains into the organic linkers<sup>40</sup>. Similarly, the hydrophilicity of the ceramic membrane was overcome after the long alkyl chains were introduced on the crosslinked graphene oxide-grafted ceramic membranes.

#### Permeability and separation performance of OD-CLGO-N-CM

The permeability of the various oils through the designed superhydrophobic ceramic membranes was evaluated for several cycles to assess the reusability and consistency of the membranes in terms of flux (Supplementary Fig. 4). Thus, hexane, octane, and hexadecane were evaluated for 10 repetitive cycles. While assessing the permeability of the various oils, the oils with lower molecular masses were observed to exhibit high permeability. The permeability of the oils decreased as their molar masses increased. The permeability of hexane was in the range of  $294 \text{ Lm}^{-2} \text{ h}^{-1}$  to  $311 \text{ Lm}^{-2} \text{ h}^{-1}$ , and hexadecane was observed in the range of  $28 \text{ Lm}^{-2} \text{ h}^{-1}$ – $33 \text{ Lm}^{-2} \text{ h}^{-1}$  (Supplementary Fig. 4). The sharp decline in the flux of hexadecane was due to its high molar mass and high viscosity. However, no significant difference in the hexane, octane, and hexadecane fluxes was observed from one cycle to the next. This result shows the robustness and stability of the membrane when dealing with various non-polar liquids.

Special wettable surfaces played a critical role in separating the water-in-oil or oil-in-water emulsions. During separation, the continuous phase must pass through the membranes. Thus, such membranes are preferred when separating the emulsions, which have a strong affinity with the continuous phase, to prevent fouling and enhance the separation efficiency of the membranes. The separation efficiency of the membranes was substantially improved by introducing special wettability behavior to the membranes<sup>41</sup>. Besides its hydrophilicity, the p-CM contains void pores, which produce a high flux when separating water-in-oil emulsions (Fig. 7). The void pores of the p-CM are visible in the SEM images (Fig. 1). The flux was substantially decreased after introducing R18-CLGO-N- on the ceramic membrane (Fig. 7d). The crosslinked graphene oxide on the ceramic membrane surface formed a separating layer. Furthermore, the graphene oxide sheets spread such that they covered the voids on the surface of the pristine ceramic membrane, resulting in a decrease in the flux of the membranes. However, the separating layer comprising R18-CLGO-N- was much more selective for oil permeation than the p-CM, which comprises hydrophilic  $\text{Al}_2\text{O}_3$  particles. The poor separation efficiency of the water-in-oil emulsions was observed for the p-CM. Figure 7b shows that the turbidity due to the presence of the emulsified water in oil is visible, and the background is tough to realize. The poor performance of the p-CM is due to two factors: (a) the presence

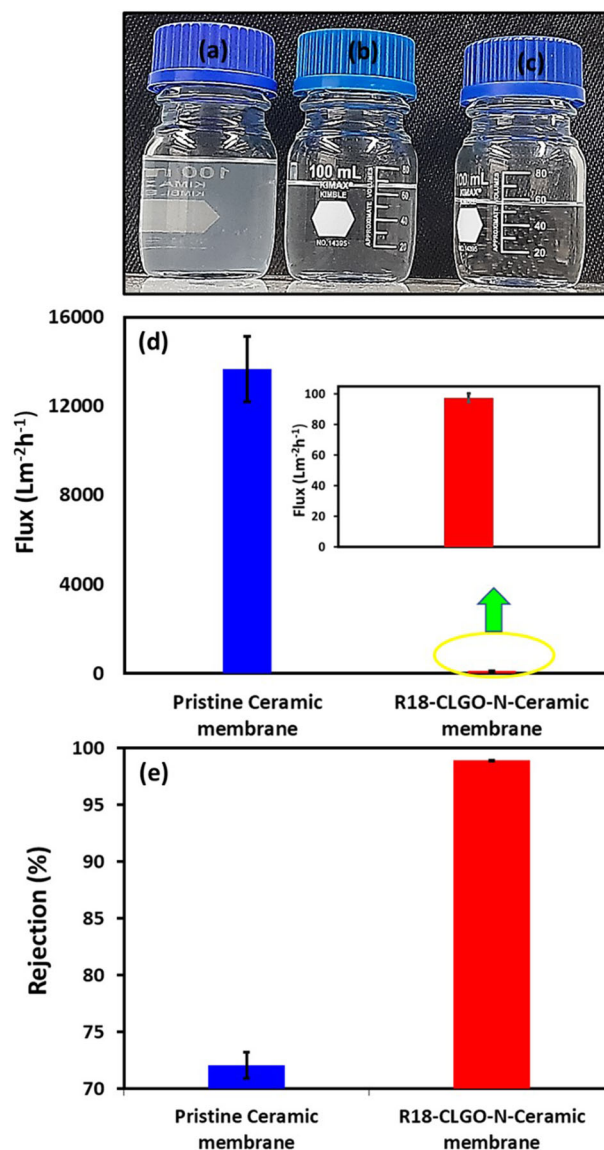


**Fig. 7 Performance of the pristine and graphene oxide-based membranes.** The camera captured images of the (a) Feed, water-in-oil emulsions, (b) permeate of the p-CM membrane, and (c) permeate of the OD-CLGO-N-CM membrane; and histograms showing the (d) permeation fluxes of the feed; and (e) separation efficiencies of ceramic membranes.

of the voids on the p-CM surface; and (b) the water-loving nature of the p-CM, which allowed the passage of water when separating the oil-in-water emulsions. The rejection of the p-CM was found at 72%, indicating its ineptitude in separating the water-in-oil emulsions. The separation efficiency was substantially enhanced up to 99% when the separation layer of the R18-CLGO-N was introduced on the ceramic membrane surface at a transmembrane pressure of 1 bar (Fig. 7e). Several factors contributed to the enhanced performance of the R18-CLGO-N-CM membranes. For example, the developed layer formed an excellent separating layer sheet with the help of graphene oxide 2D sheets to allow the effective screening of the water-in-oil emulsions. The second most critical factor was the special wettability (superhydrophobicity/superoleophilicity), which selectively allowed the passage of the oil and prevented the water from passing through the designed ceramic membranes.



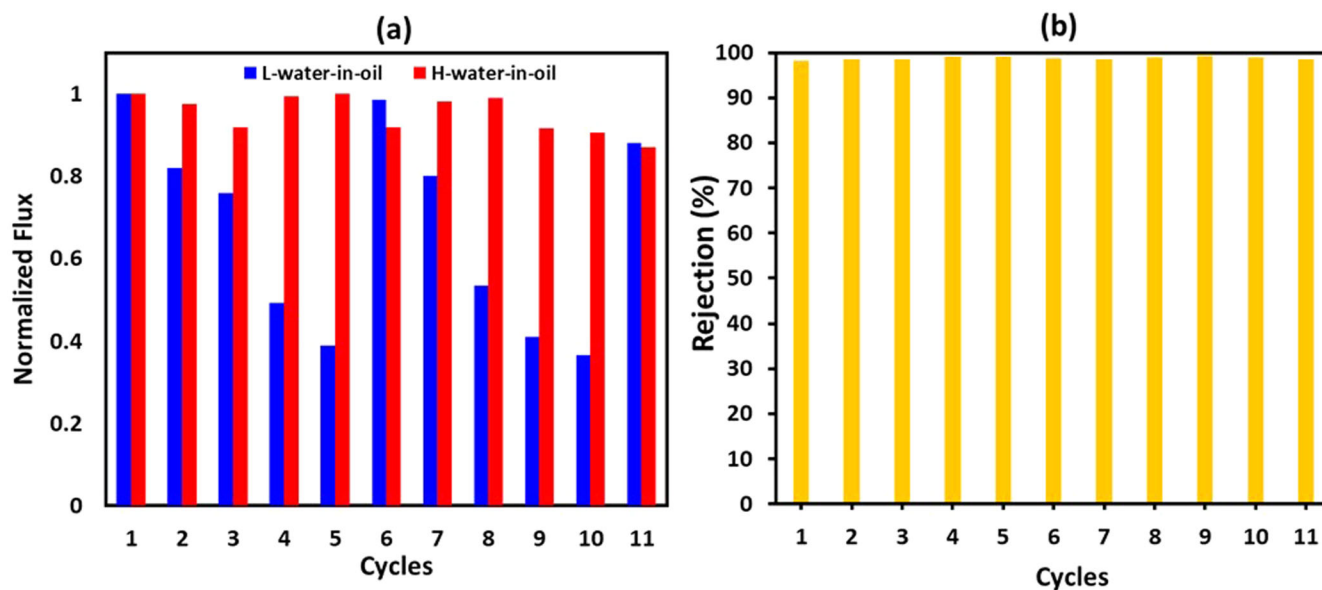


**Fig. 8** The separation performance of the membrane for different cycles. **a** Permeation flux and **(b)** separation efficiency of the R18-CLGO-N-CM membrane at different cycles while separating 1000 ppm of water-in-oil emulsions.

#### Antifouling behavior and reusability of the R18-CLGO-N-CM membrane

The fouling of the membranes when separating the oil and water emulsions has been considered a major hurdle in commercializing the membranes. The membranes are generally fouled due to gathering the oil or water and forming a compact layer. Simple methods cannot remove the foulants; thus, the membranes exhibit a poor flux recovery ratio (FRR), and the irreversibility of the flux is common. The antifouling tendency of the R18-CLGO-N-CM membrane was evaluated for 1000 ppm of H-water-in-oil emulsions (water emulsion in heavy oil) and L-water-in-oil emulsions (water emulsion in light oil). A slight, steady decrease in flux was observed while separating 1000 ppm of H-water-in-oil emulsions, and 87% of the original flux of the R18-CLGO-N-CM membrane was maintained after 11 cycles of separating the dichloromethane-in-water emulsions. For the L-water-in-oil emulsions, the situation is different. During the demulsification process, the separated water, due to its high density, forms the lower layer since the continuous phase is oil, and the overall density of the emulsions is lower than the water. This water is problematic and develops a lower layer, which acts as a barrier layer for the permeation of the oil. A similar trend was observed for the R18-CLGO-N-CM membrane while separating the L-water-in-oil emulsions. A decline in flux was observed due to water accumulation near the superhydrophobic membrane surface. By principle, the surface of the R18-CLGO-N-CM membrane should repel the water, but due to the higher density of water than hexane (light oil), it formed the lower layer and acted as a barrier layer for the permeation of light oil (Fig. 8a). It can be seen that the flux kept decreasing and reduced to <50% in the fifth cycle. Afterward, the surface cleaning was done following the simple approach of using dichloromethane.

Approximately 20 ml of DCM was added to the dead-end cell where the R18-CLGO-N-CM membrane was mounted. The DCM was kept there for 5 min. Subsequently, it was removed, and 1000 ppm of L-water-in-oil emulsions was introduced. The flux was dramatically restored to 98.5% of the original flux of the first cycle. This result indicated that the FFR of the R18-CLGO-N-CM was substantially high. Furthermore, it showed that the separated water repelled by the surface and transmembrane pressure of 1 bar was insufficient to overcome the repulsion of the surface, and the separated water was loosely present on the surface of the

R18-CLGO-N-CM. As the DCM was introduced, it immediately moved toward the membrane surface due to the strong affinity of the surface for the non-polar liquids. It immediately spreads on the surface, and being heavier than the water, the water starts to float on the DCM and is removed easily from the membrane surface. Interestingly, this issue can be easily resolved in the crossflow system. Water has fewer chances to accumulate near the surface due to the crossflow compared to the dead-end cell where the pressure is applied from one side, the permeate floats through the membrane, and separated water has no chance to move away from the surface of the superhydrophobic membranes. Furthermore, no significant impact on the rejection performance of the membrane was observed, and the membrane separation efficiency kept fluctuating in the range of 98–99.3% (Fig. 8b). The antifouling behavior and high FRR indicated that the R18-CLGO-N-CM membranes tend to deal with the H-water-in-oil and L-water-in-oil emulsions.

#### Theoretical insights on the oil–water separations using classical MD simulations

Classical MD simulations were conducted to gain theoretical insights into the oil–water separation features of the fabricated membrane. Figure 9a presents the energy-minimized amorphous cell containing five membrane units. The blue and gray isosurfaces depict the free accessible volume on the membrane at a probe radius of 1.20 Å. The membrane system was mainly stabilized by the intermolecular and intramolecular hydrogen bonds using the hydroxyl groups of the graphene oxide sheets. Using the Bondi equation<sup>42</sup>, the FFV was estimated as 0.62, indicating the compactness of the membrane layer. Meanwhile, the density field isosurface plot (Fig. 9b) further revealed moderate intramolecular free volume with low steric hindrance between the stacked layers of the graphene oxide sheets, which is sufficient for effectively separating the oil–water emulsions.

The final configurations of the dynamic simulations of the membrane–oil–water systems and their corresponding relative concentration profiles are presented in Fig. 9c–h. In the membrane–oil–water system (Fig. 9c), the membrane forms reticular interfacial films<sup>43</sup> that allow the passage of oil molecules. The water molecules could not permeate through the membrane due to polar repulsions from the dangling hydrophobic groups. In

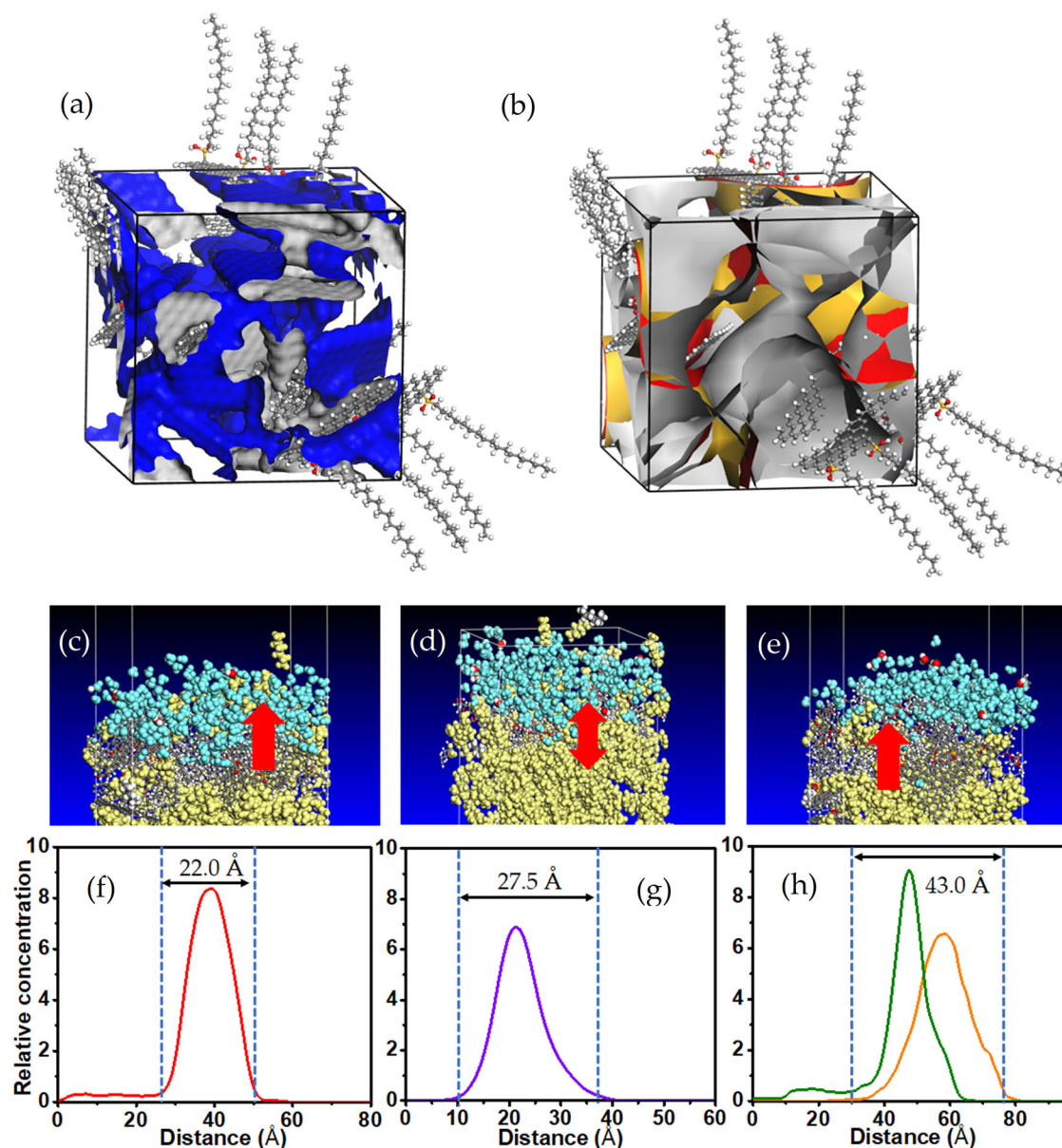


**Fig. 9** The dynamic simulation of oil–water separation. **a** The energy-minimized amorphous cell and **(b)** the density field isosurface plot of the cell comprising five units of the membrane with the Connolly surface area estimated as  $14,000 \text{ \AA}^2$ . The final geometry of the constructed oil–water interface systems, **(c)** the membrane–oil–water system, **(d)** the emulsified oil–water system, **(e)** the membrane–oil–water–surfactant system, and their corresponding relative concentration profiles **(f–h)**. The interfacial film thickness of the three systems was estimated as  $22.0$ ,  $27.5$ , and  $43.0 \text{ \AA}$ , respectively.

the emulsified oil–water system (Fig. 9d), the span-80 surfactant maintained a stable emulsion by forming a uniform monolayer at the oil–water interface with the head groups pointing toward the water phase. Meanwhile, in the membrane–oil–water surfactant system (Fig. 9e), the membrane layer forms a compact network that prevents the cross-over of water molecules while allowing the permeation of the hydrophobic oil molecules. The formation of intermolecular hydrogen bonds between the water molecules and the polar groups on the graphene oxide sheets further prevents the passage of the water molecules, increasing the oil flux. Consistent with the 90%–90% criterion<sup>44</sup>, we estimated the interfacial film thickness for the systems in Fig. 9(c), 9(d), and 9(e) to be  $22.0$ ,  $27.5$ , and  $43.0 \text{ \AA}$  (Fig. 9f–h) and the corresponding interfacial formation energy,  $E_{\text{IFE}}$ , as  $-932.6$ ,  $-1156.2$ , and  $-1643.1 \text{ kcal mol}^{-1}$ , respectively. The interfacial film thickness in the emulsified oil–water-membrane system and the

corresponding interfacial formation energy are quite high. According to the literature<sup>45</sup>, this implies the resistance of the membrane’s active layer to solvent permeation. Under the influence of the transmembrane pressure, however, the strong hydrophobic force between the active layer and the oil droplets causes the aggregation of the droplets at the membrane’s interface and the consequent permeation through the membrane pores.

Finally, we conducted dynamic simulations on the oil–water separation of the compacted membrane in a simulation box with dimensions  $49.5 \times 49.5 \times 143.6 \text{ \AA}$  with periodic boundary conditions comprising 500 molecules of hexane, 200 molecules of water, and 10 surfactant molecules in one compartment and a vacuum space of  $30 \text{ \AA}$  along the z-axis (Supplementary Fig. 5). Five membrane units were placed in the middle of the cell, and the entire system was geometrically optimized, followed by NPT and

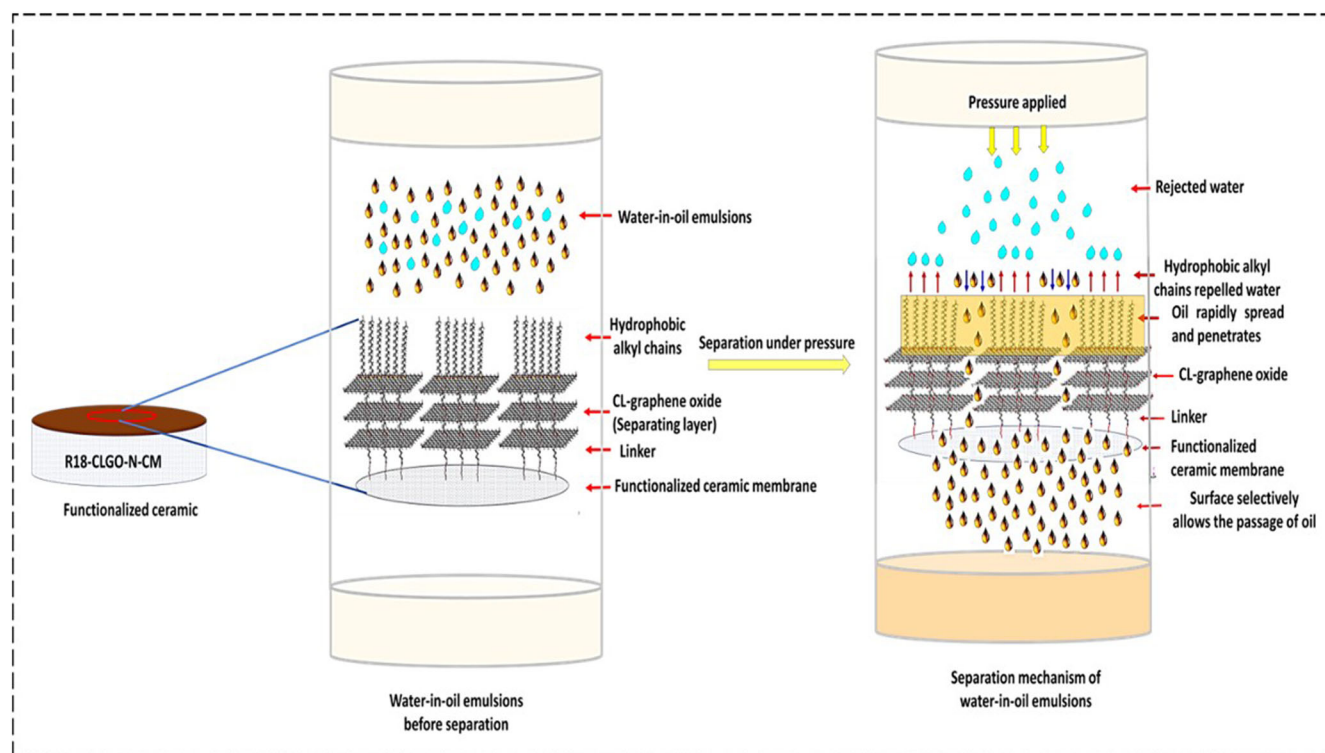


**Fig. 10 Water-in-oil emulsions separation mechanism.** Schematic representation of the mechanism of water-in-oil emulsions separation using the R18-CLGO-N-CM membrane.

NVT simulations for 500 ps each. All the simulation conditions remained the same as previously. Snapshots of the cell configurations were taken at time intervals and presented in Supplementary Fig. 6. The results suggest that the molecules approach the membrane surface and penetrate through the interfacial barrier in the first 20 ps of simulation (Supplementary Fig. 6a). At 50–100 ps (Supplementary Fig. 6b and c), the oil molecules begin to diffuse to the vacuum compartment while the water molecules remain trapped in the oil–water interface. Few molecules of water were able to overcome the interfacial barrier by continuous accumulation along the polar groups on the graphene oxide layers, thus weakening the hydrogen bond (Supplementary Fig. 6d). Thus, it appears from the kinetic perspective that the permeation rate of the oil molecules through the membrane was more energetically favored than the water molecules, which have to overcome a substantial interfacial energy barrier. Altogether, the results of the classical MD simulations predicted that the membrane in our study exhibits excellent oil–water separation efficiency and could be further explored. The mechanism of the water-in-oil emulsion separation is shown in Fig. 10.

In summary, superhydrophobic ceramic membranes were developed using crosslinked graphene oxide, which was grafted on the surface of the ceramic membrane using  $N^1$ -(3-Trimethoxysilylpropyl)diethylenetriamine. The surface energy of the cross-linked graphene oxide was reduced by functionalizing with octadecyl contributed from  $C_{18}H_{37}Cl_3Si$ , which turned the ceramic membrane surface superhydrophobic. The ceramic membrane, which was super hydrophilic at a water contact angle of  $0^\circ$  and oleophobic underwater ( $141.3^\circ \pm 1.5^\circ$ ), turned superhydrophobic at a water contact angle of  $152.8^\circ \pm 0.6^\circ$  and an underwater oil contact angle of  $0^\circ$ . This phenomenon showed the high special wettability and the selectivity of the R18-CLGO-N-CM membrane. High flux was observed for non-polar liquids, and hexane was found in the range of  $294 \text{ Lm}^{-2}\text{h}^{-1}$ – $311 \text{ Lm}^{-2}\text{h}^{-1}$ . We found that the flux declined as the molar mass and viscosity of the non-polar liquids increased. The rationally grafted separating layer on the

surface of the ceramic membrane demonstrated a separation efficiency of  $\sim 99\%$  while treating 1000 ppm of water-in-oil emulsions at a transmembrane pressure of 1 bar, with an excellent flux of  $97 \text{ Lm}^{-2}\text{h}^{-1}$ . The R18-CLGO-N-CM exhibited excellent antifouling behavior when separating the H-water-in-oil emulsions, and the FFR was found at about 98.5% for L-water-in-oil emulsions. The flux recovery was achieved using dichloromethane, which pushed the water up from the surface and restored the ceramic membrane flux. Thus, the superb separation efficiencies, high flux, and excellent antifouling characteristics of the functionalized graphene oxide–grafted ceramic membrane make it an exceptional candidate for separating water-in-oil emulsions.

## METHODS

### Materials

Alumina ceramic disc membranes with a diameter of 4.7 cm and an average pore size of  $0.5 \mu\text{m}$  were acquired from Lianyung Highborn Technology Ltd. Graphene oxide (4 mg/mL), organosilicon ( $C_{18}H_{37}Cl_3Si$ ), Pentane-1,5-dial solution (25%),  $N^1$ -(3-Trimethoxysilylpropyl)diethylenetriamine, HCl, Span<sup>®</sup> 80, and hexane were purchased from Sigma Aldrich. Dichloromethane was obtained from Merck. Deionized water, produced with a resistance of  $18.2 \text{ M}\Omega$  from a PURELAB flex, was used for preparation of water-in-oil emulsions.

### Instrumentation

Membrane morphological analysis was performed using a Thermo Scientific<sup>™</sup> Quattro field-emission scanning electron microscope (SEM). A drop shape analyzer (DSA25, KRÜSS) was used to measure the water contact angle and surface wettability of the ceramic membranes. A Nicolet 6700 Fourier transform infrared spectroscopy (FTIR) instrument was used for FTIR analysis of the membranes. A PURELAB flex was used for deionized water



collection and a Sterlitech dead-end filtration cell was used to test various pristine and functionalized membranes.

### Functionalized ceramic membrane design

The ceramic membranes were placed in a 1% solution of N1-(3-Trimethoxysilylpropyl)diethylenetriamine prepared in ethanol for 4 h. The ceramic membranes were then taken out and placed into an oven at 110 °C for condensation from the N-CM membrane. A 0.12 mg/mL graphene oxide solution was prepared and Pentane-1,5-dial was added to achieve a final solution concentration of 1%. A few drops of HCl were added to catalyze crosslinking of the graphene oxide nanosheets. The graphene oxide solution along the pentane-1,5-dial was stirred for 12 h at room temperature. The N-CM membrane was fitted into a dead-end cell and 30 mL of graphene oxide solution was passed through it at an applied pressure of 1 bar to form CLGO-N-CM. Next, the CLGO-N-CM was taken out of the cell, kept at room temperature until completely dried, and then placed in a 1% organosilicon (C18H37Cl3Si) solution prepared in toluene for 4 h. Then, the CLGO-N-CM was washed thoroughly with ethanol to remove the loosely held R18-alkyl chains, leaving only those covalently linked to the surface. After washing, the R18-CLGO-N-CM membranes were stored at room temperature for further testing of water-in-oil emulsion separation efficiency.

### Separation of water-in-oil emulsions

Using Span® 80 for stabilization, 1000 ppm water-in-oil emulsions were prepared. The calculated amount of water was added to n-Hexane, which was kept stirring in the presence of Span® 80 at 800 rpm for 48 h. Milky-color water-in-oil emulsions were obtained using water and hexane. The separation efficiency was calculated using Eq. (4):<sup>46</sup>

$$\eta = \left(1 - \frac{C_p}{C_f}\right) \times 100 \quad (4)$$

where  $\eta$  represents the separation efficiency,  $C_f$  represents the water concentration in the feed, and  $C_p$  indicates the water concentration in the permeate.

The permeation flux of the pristine and the functionalized ceramic membranes was calculated using Eq. (5):

$$J = \Delta V / A \times \Delta t \quad (5)$$

where  $J$  represents the permeation flux,  $\Delta t$  is the permeation time (h),  $A$  is the membrane effective surface area (m<sup>2</sup>), and  $\Delta V$  is the collected volume of permeate (L). The error bars in the represented graphs show the acquired data's standard deviation (SD).

### Molecular dynamics simulations

Molecular dynamics (MD) simulations were accomplished using the Materials Studio 8.0 suite using the Forcite module and the COMPASS II forcefield. This forcefield was chosen as it provides extended coverage of the COMPASS forcefield to polymers and heterocyclic systems, and often yields results consistent with experimental findings<sup>47,48</sup>. In order to minimize the computational cost, the active membrane layer was simplified throughout the simulations, as presented in Supplementary Fig. 7. The membrane density and fractional free volume (FFV) were determined by constructing a cubic amorphous cell with lattices 42.0 × 42.0 × 42.0 Å, comprising five membrane units. The constructed cell was minimized via geometry optimization, followed by constant pressure and temperature (NPT) and constant volume and temperature (NVT) dynamics simulations each for 1000 ps at a time step of 0.001 ps. The Nose–Hoover thermostat and the Berendsen barostat were used to control the temperature and pressure. Long-range Coulombic interactions were treated using the Ewald summation method, whereas the Lennard–Jones attractive and repulsive interactions were estimated at a cut-off range of 18.5 Å.

To study the stability at the oil/water interface, molecules of water, the emulsifier (Span-80), the membrane active layer, and the hexane molecules, which were chosen as the oil model, were geometrically optimized and followed by 5 ps (5000 steps) of simulated annealing to obtain the ground state molecular configurations. Three symmetric cells were constructed, indicated by (a), (b), and (c) in Supplementary Fig. 8, which are comprised of (a) 500 molecules of hexane, 200 molecules of water, and 5 membrane active units with the membrane placed at the oil/water interface, (b) 500 molecules of hexane, 200 molecules of water, and 10 units of Span-80 with the emulsifier placed at the oil–water interface, and (c) 500 molecules of hexane, 200 molecules of water, 10 units of Span-80 and 5 membrane units with the membrane placed near the oil. The lattices of the three constructed cells were 46.7 × 46.7 × 121.4 Å, 46.7 × 46.7 × 75.9 Å, and 46.7 × 46.7 × 130.2 Å for models (a), (b), and (c), respectively. All the systems were subjected to energy minimizations with the convergence tolerance set to ultrafine, followed by equilibration at 298.0 K for 500 ps on an NPT ensemble and NVT dynamics simulation for 1000 ps with periodic boundary conditions at a time step of 0.001 ps. The simulation conditions remain the same, as mentioned earlier. The interfacial formation energy ( $E_{IFE}$ ), which describes the oil–water interface stability, was calculated using Eq. (6):

$$E_{IFE} = \frac{1}{2} [E_{system} - (E_{membrane} + E_{surfactant} + E_{oil-water})] \quad (6)$$

where  $E_{system}$  (kcal/mol) represents the total energy of the configuration under study,  $E_{surfactant}$  (kcal/mol) is the energy of the Span-80 surfactant,  $E_{membrane}$  (kcal/mol) is the energy of the membrane active layer in the studied configuration, and  $E_{oil-water}$  (kcal/mol) represents the total energy of the oil–water system.

### DATA AVAILABILITY

All data generated or analyzed during this study are included in this published paper, and its supplementary information files.

Received: 26 September 2022; Accepted: 2 May 2023;

Published online: 15 May 2023

### REFERENCES

- Zhang, W. et al. Superhydrophobic and superoleophilic PVDF membranes for effective separation of water-in-oil emulsions with high flux. *Adv. Mater.* **25**, 2071–2076 (2013).
- Ekins, P., Vanner, R. & Firebrace, J. Zero emissions of oil in water from offshore oil and gas installations: economic and environmental implications. *J. Clean. Prod.* **15**, 1302–1315 (2007).
- Yang, C. et al. Fabrication of a PPS microporous membrane for efficient water-in-oil emulsion separation. *Langmuir* **34**, 10580–10590 (2018).
- Xu, H., Liu, H., Huang, Y. & Xiao, C. Three-dimensional structure design of tubular polyvinyl chloride hybrid nanofiber membranes for water-in-oil emulsion separation. *J. Memb. Sci.* **620**, 118905 (2021).
- Baig, N., Salhi, B., Sajid, M. & Aljundi, I. H. Recent progress in microfiltration/ultrafiltration membranes for separation of oil and water emulsions. *Chem. Rec.* e202100320 <https://doi.org/10.1002/TCR.202100320> (2022).
- Kota, A. K., Kwon, G., Choi, W., Mabry, J. M. & Tuteja, A. Hygro-responsive membranes for effective oil–water separation. *Nat. Commun.* **3**, 1–8 (2012).
- Baig, N. et al. Antifouling low-pressure highly permeable single step produced loose nanofiltration polysulfone membrane for efficient Erichrome Black T/divalent salts fractionation. *J. Environ. Chem. Eng.* **10**, 108166 (2022).
- Al-Husaini, I. S., Yusoff, A. R. M. & Wirzal, M. D. H. Efficient oil/water separation using superhydrophilic polyethersulfone electrospun nanofibrous ultrafiltration membranes. *J. Environ. Chem. Eng.* **10**, 108341 (2022).
- Cabrera, S. M. et al. Performance evaluation of an industrial ceramic nanofiltration unit for wastewater treatment in oil production. *Water Res.* **220**, 118593 (2022).
- Chen, W. et al. Separation of oil/water emulsion using pluronic F127 modified polyethersulfone ultrafiltration membranes. *Sep. Purif. Technol.* **66**, 591–597 (2009).
- Wang, J.-W., Abadikhah, H., Wang, F.-H., Yin, L.-J. & Xu, X.  $\beta$ -silicon nitride membrane with robust inorganic-organic hybrid hydrophobic surface for water-

- in-oil emulsion separation. *Ceram. Int.* <https://doi.org/10.1016/J.CERAMINT.2022.03.027> (2022).
12. Hu, X. et al. The improved oil/water separation performance of graphene oxide modified Al<sub>2</sub>O<sub>3</sub> microfiltration membrane. *J. Memb. Sci.* **476**, 200–204 (2015).
  13. Zou, D. et al. One-step engineering of low-cost kaolin/fly ash ceramic membranes for efficient separation of oil-water emulsions. *J. Memb. Sci.* **621**, 118954 (2021).
  14. Marzouk, S. S., Naddedeo, V., Banat, F. & Hasan, S. W. Preparation of TiO<sub>2</sub>/SiO<sub>2</sub> ceramic membranes via dip coating for the treatment of produced water. *Chemosphere* **273**, 129684 (2021).
  15. Li, H., Mu, P., Li, J. & Wang, Q. Inverse desert beetle-like ZIF-8/PAN composite nanofibrous membrane for highly efficient separation of oil-in-water emulsions. *J. Mater. Chem. A Mater.* **9**, 4167–4175 (2021).
  16. Zhang, J., Liu, L., Si, Y., Yu, J. & Ding, B. Rational design of electrospun nanofibrous materials for oil/water emulsion separation. *Mater. Chem. Front.* **5**, 97–128 (2021).
  17. Wei, Y., Qi, H., Gong, X. & Zhao, S. Specially wettable membranes for oil–water separation. *Adv. Mater. Interfac.* **5**, 1800576 (2018).
  18. Wang, M., Peng, M., Zhu, J., Li, Y. D. & Zeng, J. B. Mussel-inspired chitosan modified superhydrophilic and underwater superoleophobic cotton fabric for efficient oil/water separation. *Carbohydr. Polym.* **244**, 116449 (2020).
  19. Baig, N. & Saleh, T. A. A facile development of superhydrophobic and superoleophilic micro-textured functionalized mesh membrane for fast and efficient separation of oil from water. *J. Environ. Chem. Eng.* **9**, 105825 (2021).
  20. Wang, X. et al. Preparation of superhydrophilic/underwater superoleophobic membranes for separating oil-in-water emulsion: mechanism, progress, and perspective. *J. Coat. Technol. Res.* **18**, 285–310 (2021).
  21. Rasouli, S., Rezaei, N., Hamed, H., Zendejboudi, S. & Duan, X. Superhydrophobic and superoleophilic membranes for oil-water separation application: a comprehensive review. *Mater. Des.* **204**, 109599 (2021).
  22. Picard, C., Larbot, A., Tronel-Peyroz, E. & Berjoan, R. Characterisation of hydrophilic ceramic membranes modified by fluoroalkylsilanes into hydrophobic membranes. *Solid State Sci.* **6**, 605–612 (2004).
  23. Lu, D. et al. Hydrophilic Fe<sub>2</sub>O<sub>3</sub> dynamic membrane mitigating fouling of support ceramic membrane in ultrafiltration of oil/water emulsion. *Sep. Purif. Technol.* **165**, 1–9 (2016).
  24. Wei, Y., Xie, Z. & Qi, H. Superhydrophobic-superoleophilic SiC membranes with micro-nano hierarchical structures for high-efficient water-in-oil emulsion separation. *J. Memb. Sci.* **601**, 117842 (2020).
  25. Lin, J. C., Lee, D. J. & Huang, C. Membrane fouling mitigation: membrane cleaning. *Sep. Sci. Technol.* **45**, 858–872 (2010).
  26. Kang, L., Zhao, L., Yao, S. & Duan, C. A new architecture of super-hydrophilic β-SiAlON/graphene oxide ceramic membrane for enhanced anti-fouling and separation of water/oil emulsion. *Ceram. Int.* **45**, 16717–16721 (2019).
  27. Shahzad, A. et al. Advances in the synthesis and application of anti-fouling membranes using two-dimensional nanomaterials. *Membranes* **11**, 605 (2021).
  28. Deng, S. & Berry, V. Wrinkled, rippled and crumpled graphene: an overview of formation mechanism, electronic properties, and applications. *Mater. Today* **19**, 197–212 (2016).
  29. Baig, N., Saleh, T. A., Baig, N. & Saleh, A. Superhydrophobic polypropylene functionalized with nanoparticles for efficient fast static and dynamic separation of spilled oil from water. *Glob. Chall.* **3**, 1800115 (2019).
  30. Romero Toledo, R., Ruiz Santoyo, V., Moncada Sánchez, D. & Martínez Rosales, M. Effect of aluminum precursor on physicochemical properties of Al<sub>2</sub>O<sub>3</sub> by hydrolysis/precipitation method. *Nova Sci.* **10**, 83–99 (2018).
  31. Nijem, N. et al. Water cluster confinement and methane adsorption in the hydrophobic cavities of a fluorinated metal-organic framework. *J. Am. Chem. Soc.* **135**, 12615–12626 (2013).
  32. Gu, Q. et al. Chemical-grafting of graphene oxide quantum dots (GOQDs) onto ceramic microfiltration membranes for enhanced water permeability and anti-organic fouling potential. *Appl. Surf. Sci.* **502**, 144128 (2020).
  33. Baig, N., Kawde, A. N. & Ibrahim, M. Efficient ionic medium supported reduced graphene oxide-based sensor for selective sensing of dopamine. *Mater. Adv.* **1**, 783–793 (2020).
  34. Baig, N. & Kawde, A. N. A novel, fast and cost effective graphene-modified graphite pencil electrode for trace quantification of L-tyrosine. *Anal. Methods* **7**, 9535–9541 (2015).
  35. Sudesh, Kumar, N., Das, S., Bernhard, C. & Varma, G. D. Effect of graphene oxide doping on superconducting properties of bulk MgB<sub>2</sub>. *Supercond. Sci. Technol.* **26**, 095008 (2013).
  36. Valencia, C. et al. Synthesis and application of scaffolds of chitosan-graphene oxide by the freeze-drying method for tissue regeneration. *Molecules* **23**, 2651 (2018).
  37. Saharudin, K. A. et al. Improved super-hydrophobicity of eco-friendly coating from palm oil fuel ash (POFA) waste. *Surf. Coat. Technol.* **337**, 126–135 (2018).
  38. Wei, Y., Qi, H., Gong, X. & Zhao, S. Specially wettable membranes for oil–water separation. *Adv. Mater. Interfac.* **5**, 1800576 (2018).
  39. Chenxi, Y. et al. Novel fabrication of hydrophobic/oleophilic human hair fiber for efficient oil/water separation through one-pot dip-coating synthesis route. *Sci. Rep.* **12**, 1–10 (2022).
  40. Zhu, N.-X. et al. Self-generation of surface roughness by low-surface-energy alkyl chains for highly stable superhydrophobic/superoleophilic MOFs with multiple functionalities. *Angew. Chem.* **131**, 17189–17196 (2019).
  41. Ma, Q., Cheng, H., Fane, A. G., Wang, R. & Zhang, H. Recent development of advanced materials with special wettability for selective oil/water separation. *Small* **12**, 2186–2202 (2016).
  42. Bondi, A. Van der waals volumes and radii. *J. Phys. Chem.* **68**, 441–451 (1964).
  43. Li, X., Kersten, S. R. A. & Schuur, B. Efficiency and mechanism of demulsification of oil-in-water emulsions using ionic liquids. *Energy Fuels* **30**, 7622–7628 (2016).
  44. Jang, S. S. et al. Molecular dynamics study of a surfactant-mediated decane –water interface: effect of molecular architecture of alkyl benzene sulfonate. *J. Phys. Chem. B* **108**, 12130–12140 (2004).
  45. Duan, M. et al. Synthesis of a novel copolymer of block polyether macromonomer and diallyldimethylammonium chloride and its reverse demulsification performance. *J. Pet. Sci. Eng.* **175**, 317–323 (2019).
  46. Wang, Y. et al. An integrated strategy for achieving oil-in-water separation, removal, and anti-oil/dye/bacteria-fouling. *Chem. Eng. J.* **413**, 127493 (2021).
  47. Sun, H. et al. COMPASS II: extended coverage for polymer and drug-like molecule databases. *J. Mol. Model.* **22**, 1–10 (2016).
  48. Abdulazeez, I., Salhi, B., Baig, N. & Peng, Q. The role of sulphonic and phosphoric pendant groups on the diffusion of monovalent ions in polyelectrolyte membranes: a molecular dynamics study. *Membranes* **11**, 940 (2021).

## ACKNOWLEDGEMENTS

The authors would like to acknowledge the support provided by the Deanship of Research Oversight and Coordination and Interdisciplinary Research Center for Membranes & water security through project No. INMW2312 King Fahd University of Petroleum and Minerals.

## AUTHOR CONTRIBUTIONS

N.B.: Conceptualization, investigation, data curation, writing part of original draft; I.A.: Investigation, methodology, writing-review; I.A.: Conceptualization, writing part of the original draft, and editing.

## COMPETING INTERESTS

The authors declare no competing interests.

## ADDITIONAL INFORMATION

**Supplementary information** The online version contains supplementary material available at <https://doi.org/10.1038/s41545-023-00252-y>.

**Correspondence** and requests for materials should be addressed to Nadeem Baig.

**Reprints and permission information** is available at <http://www.nature.com/reprints>

**Publisher's note** Springer Nature remains neutral with regard to jurisdictional claims in published maps and institutional affiliations.



**Open Access** This article is licensed under a Creative Commons Attribution 4.0 International License, which permits use, sharing, adaptation, distribution and reproduction in any medium or format, as long as you give appropriate credit to the original author(s) and the source, provide a link to the Creative Commons license, and indicate if changes were made. The images or other third party material in this article are included in the article's Creative Commons license, unless indicated otherwise in a credit line to the material. If material is not included in the article's Creative Commons license and your intended use is not permitted by statutory regulation or exceeds the permitted use, you will need to obtain permission directly from the copyright holder. To view a copy of this license, visit <http://creativecommons.org/licenses/by/4.0/>.

© The Author(s) 2023